JACS
JOURNAL OF THE AMERICAN CHEMICAL SOCIETY

pubs.acs.org/JACS

Article

# Spatiotemporal Resolution of Conformational Changes in Biomolecules by Combining Pulsed Electron−Electron Double Resonance Spectroscopy with Microsecond Freeze-Hyperquenching

Tobias Hett,[‡] Tobias Zbik,[‡] Shatanik Mukherjee, Hideto Matsuoka, Wolfgang Bönigk, Daniel Klose, Christophe Rouillon, Norbert Brenner, Sebastian Peuker, Reinhard Klement, Heinz-Jürgen Steinhoff, Helmut Grubmüller, Reinhard Seifert, Olav Schiemann,* and U. Benjamin Kaupp*

Cite This: *J. Am. Chem. Soc.* 2021, 143, 6981−6989

Read Online

ACCESS | Metrics & More | Article Recommendations | Supporting Information

**ABSTRACT:** The function of proteins is linked to their conformations that can be resolved with several high-resolution methods. However, only a few methods can provide the temporal order of intermediates and conformational changes, with each having its limitations. Here, we combine pulsed electron−electron double resonance spectroscopy with a microsecond freeze-hyperquenching setup to achieve spatiotemporal resolution in the angstrom range and lower microsecond time scale. We show that the conformational change of the $C_\alpha$-helix in the cyclic nucleotide-binding domain of the *Mesorhizobium loti* potassium channel occurs within about 150 $\mu$s and can be resolved with angstrom precision. Thus, this approach holds great promise for obtaining 4D landscapes of conformational changes in biomolecules.

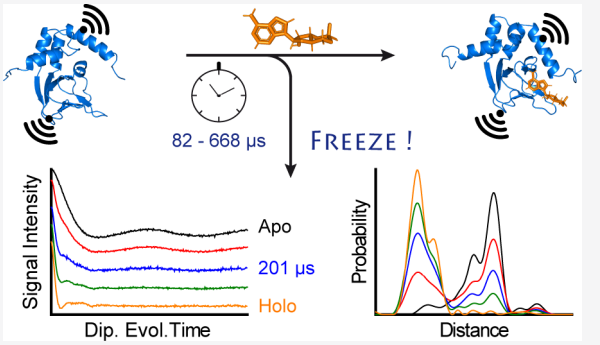


## INTRODUCTION

The function of biomolecules is intimately linked to their structure and dynamics. Often, effector-triggered conformational changes are key to protein function. Membrane-spanning proteins such as G protein-coupled receptors or ion channels, which are particularly challenging for structural biology,[1,2] exist in active and inactive conformations. The transition between active and inactive form is triggered by ligand binding[3−6] or physical cues such as changes in membrane voltage,[7] absorption of light,[8,9] or mechanical forces.[10] These conformational changes happen on different length and time scales ranging from angstrom to nanometers, and picoseconds to seconds.[11] X-ray crystallography, NMR spectroscopy, and electron microscopy greatly advanced our knowledge about structures and their dynamics. Here, we introduce a combination of pulsed electron−electron double resonance spectroscopy (PELDOR or DEER)[12−14] with so-called microsecond freeze-hyperquenching (MHQ) as a complementary technique (MHQ/PELDOR) to achieve a 4D conformational landscape from the initial to the final conformational state with high spatiotemporal resolution.

PELDOR yields ensemble distributions of distances between electron-spin centers in frozen samples in the range of 1.5 to 16 nm with angstrom precision.[15] In biomolecules, spin centers can be introduced via site-directed spin labeling (SDSL) of, for example, cysteine residues in proteins by means of nitroxide spin labels.[16] Combining SDSL and PELDOR, the structures and conformational changes of large proteins,[12,17,18] oligonucleotides,[19−21] and protein/oligonucleotide complexes[22−26] have been studied in solution,[27,28] in membranes,[29−32] or even whole cells.[33−36] Although PELDOR provides information on the conformational ensemble present at the freezing point,[37,38] it is blind to the time scales and sequence of conformational events.

However, coupling SDSL/PELDOR with fast freeze-quench techniques[39] may permit taking snapshots along the trajectory of a conformational change and provide access to the time domain with temporal resolution only limited by the mixing and freezing kinetics. The time scale of protein dynamics ranges from femtoseconds for bond vibrations via nano- and microseconds for movements of $\alpha$-helices and $\beta$-sheets, up to seconds or even hours for folding and assembly of multisubunit proteins.[11] Ligand-induced conformational changes are of particular interest, as they trigger important cellular reactions, and the rate-limiting steps are often unknown. To follow such movements in proteins, mixing and freeze-quenching should be completed within microseconds. While

**Received:** February 5, 2021
**Published:** April 27, 2021

typical freeze-quench setups operate on a millisecond time scale,[40,41] an MHQ device can reach minimal aging times of roughly 100 $\mu$s.[39] MHQ combined with continuous wave (CW) electron paramagnetic resonance (EPR) has been used to examine the binding kinetics of the azide/metmyoglobin system,[39] the lifetime of catalytic intermediates,[42−44] the refolding of cytochrome oxidases,[45] and the electron-transfer rates in the respiratory complex I.[46] Two previous studies have employed freeze-quench/PELDOR to test the distance distribution width with respect to the freezing time.[37,38] Ligand-activated conformational motions, however, have so far not been studied by MHQ, which extends the time scale from milli- to microseconds.

Here we study the ligand-induced conformational dynamics of the bacterial cyclic nucleotide-gated (CNG) $K^+$ channel from *Mesorhizobium loti* (MloK1), which opens by binding of cyclic adenosine monophosphate (cAMP) to a cyclic nucleotide-binding domain (CNBD).[47,48] Upon binding, the CNBD undergoes a conformational change, including a movement of the C-terminal $C_\alpha$-helix (Figure 1). This

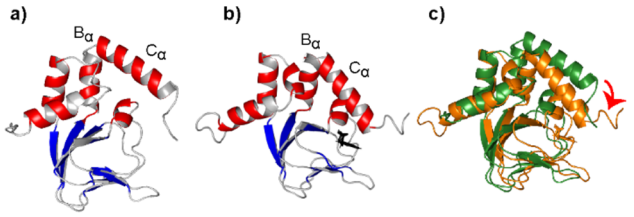


**Figure 1.** Structure of the CNBD of the MloK1 channel. (a) Structure of the ligand-free *apo* state (PDB-ID: 2kxl) and (b) the cAMP-bound *holo* state (PDB-ID: 2k0g). (c) Overlay of both structures (*apo* in green, *holo* in orange) illustrating the $C_\alpha$-helix movement upon ligand binding (red arrow).

movement has been inferred from X-ray[49] and NMR[50,51] structures of the CNBD in its *apo* and *holo* states and has also been predicted by atomistic simulations.[52] A similar movement has been detected with PELDOR in a related hyperpolarization-activated and cyclic nucleotide-gated channel (HCN2)[53] and the bacterial CNG channel SthK.[54]

We will show that MHQ/PELDOR can resolve conformational changes of the MloK1 CNBD on the angstrom and low-microsecond time scale. In addition, placing spin labels at different sites in the CNBD can provide a 4D picture of a conformational change with amino-acid resolution.

## EXPERIMENTAL SECTION

The MHQ device is based on a prototype reported by de Vries' group (Figure S1).[39] It consists of a rotating aluminum cold-plate, a vacuum hood, and two syringes connected by tubing to a four-jet tangential micromixer. The protein and ligand solutions are injected from syringes via tubing into the micromixer. The mixture is ejected from the micromixer as a free-flowing thin jet (diameter: 20 $\mu$m) that is freeze-quenched within microseconds on a rotating cold-plate. The micromixer is mounted on a robotic swivel arm that allows vertical and horizontal movements. Vertical movement ascertains that the entire cold-plate surface is optimally used for freezing; horizontal movement sets the distance between micromixer and cold-plate and, thereby, the aging time, $t_a$.

The aging time $t_a$ consists of three components: the mixing time $t_m$ (residence time in the micromixer), the transport time $t_t$ (time-of-flight in the jet), and the quenching or freezing time $t_q$ (SI Section 1.1).[39,41]

$$t_a = t_m + t_t + t_q$$

The time $t_m$ is determined by the mixer volume and the flow rate during mixing. The time $t_q$ depends on the jet diameter as well as the heat conductivity of the aqueous sample and the cold-plate material.[37,39] The diameter of the jet, known from the orifice diameter, and the volumetric flow rate yield a $t_m$ of 1 $\mu$s and a $t_q$ of approximately 40 $\mu$s.[39] The transport time $t_t$ is set by the jet velocity and the distance between the mixer orifice and the cold-plate.[39] Its lower limit is given by a safe minimal distance between the orifice and the cold-plate of about >2 mm (SI Section 1.1). Microsecond quenching requires high linear flow rates (up to 200 m $s^{-1}$) achieved by HPLC pumps. Small uniform jet diameters are obtained by operating the mixer and the cold-plate under a vacuum hood. The vacuum prevents jet breakup and ensures that experimental and theoretically expected transport times match. The actual transport time $t_t$, as demonstrated by laser Doppler anemometry, is only <10% shorter than the value calculated from flow rates.[39] The shortest aging time $t_a$ achieved was 82 $\mu$s (Table S1).

## RESULTS

**Calibration of the MHQ Device.** The reaction kinetics between equine heart metmyoglobin (MetMb) and sodium azide ($NaN_3$)[55] was employed to calibrate the MHQ aging times. In the *apo* state, the Fe(III) ion in the heme group is in the *high*-spin state ($S$ = 5/2, abbreviated *hs*), and binding of azide switches it to the *low*-spin state ($S$ = 1/2, abbreviated *ls*). *Hs*- and *ls* Fe(III) give rise to an apparent axial ($g_{xx} = g_{yy}$ = 5.8, $g_{zz}$ = 2.0) and orthorhombic EPR spectrum ($g_{zz}$ = 2.8, $g_{yy}$ = 2.2, $g_{xx}$ = 1.8),[56,57] respectively, which allows following the progression of the reaction by CW EPR spectroscopy (Figure 2).

The reaction gradually progressed with the aging time (Figure 2c,d, Extended Data Figure 1, SI Section 9.1). The signal intensities of *hs* Fe(III) at $g_{xx} = g_{yy}$ = 5.8 decreased with $t_a$, whereas the intensities of the *ls* state ($g_{zz}$ = 2.8 and $g_{yy}$ = 2.2) concomitantly increased (Figure 2c). The fraction of *hs* and *ls* state trapped in the frozen sample at an aging time $t_a$ can be deduced from the peak-to-peak intensities of the respective signals in the CW EPR spectra (Figure 2c and SI Section 4.5). These fractions were fitted by two exponentials $y = ae^{-k_1't} + be^{-k_2't}$ with pseudo-first-order rate constants $k_1'$ = 19 669 ± 5406 $s^{-1}$ and $k_2'$ = 1358 ± 189 $s^{-1}$ (Figure 2d). These rate constants k′ translate into second-order rate constants $k_1$ = 26 225 ± 7208 $M^{-1}$ $s^{-1}$ and $k_2$ = 1811 ± 253 $M^{-1}$ $s^{-1}$, which are in good agreement with previous accounts (Table S2).[39]

The biphasic behavior may be attributed to different reactions occurring in parallel, e.g., binding of $N_3^-$ and $HN_3$, or temperature drifts depending on the length of the jet.[39] The dispersion of the $y$-values (coefficient of variation = SD/mean) (Figure 2d) was maximally 17% for $t_a$ = 82 $\mu$s and ranged between 0.6% and 8.0% for all other data points. Thus, for our purpose, reliable aging times as short as 82 $\mu$s and up to 668 $\mu$s can be obtained with the MHQ device, yet the operational range is much larger (<20 ms).

**MHQ/PELDOR Can Resolve Movements in the CNBD of the MloK1 Channel.** The *apo* state of the MloK1 CNBD undergoes a cAMP-induced conformational change (Figure 1), the most prominent being a movement of the $C_\alpha$-helix[49−51] (NMR structures: PBD-IDs: 2kxl, *apo* and 2k0g, *holo*[50] and crystal structures: PDB-IDs: 1u12, *apo* and 1vp6, *holo*[49]).

Based on the *apo* and *holo* state structures, sites for labeling with the nitroxide spin label *S*-(1-oxyl-2,2,5,5-tetramethylpyrroline-3-methyl)methanethiosulfonate (MTSSL) were chosen


https://doi.org/10.1021/jacs.1c01081
J. Am. Chem. Soc. 2021, 143, 6981−6989

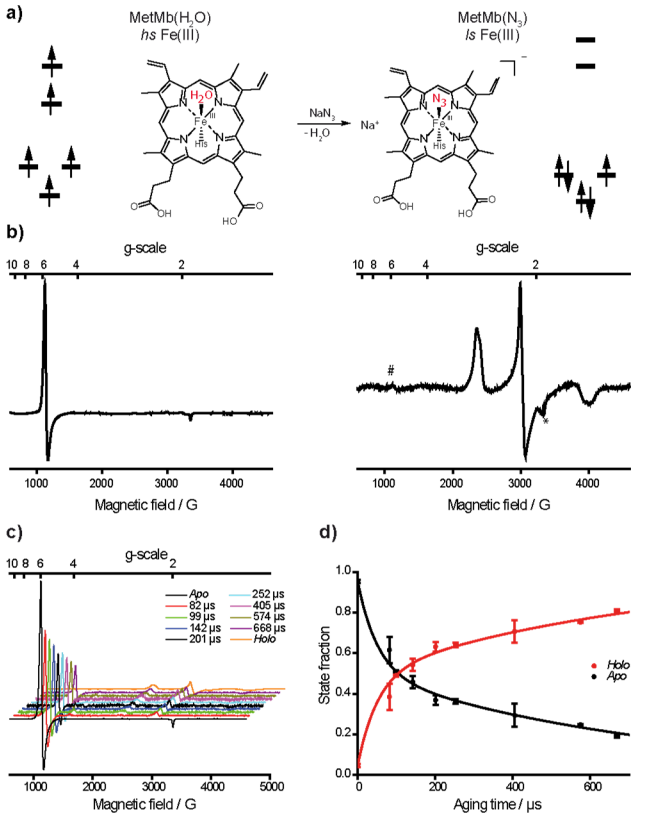


**Figure 2.** Reaction between MetMb and $NaN_3$ converting Fe(III) from the *hs* to the *ls* state. (a) Lewis structures of the *hs* and *ls* states. For clarity, only the porphyrin ring of MetMb is shown. Orbital diagrams indicate the occupation of $t_{2g}$ and $e_g$ orbitals in the octahedral ligand field for either the *hs* or *ls* state. (b) Continuous-wave X-band (9.4 GHz) EPR spectra recorded at 20 K of MetMb in the *hs* state (left) and the *ls* state (right). In the spectrum of the *ls* state, a residual of the *hs* Fe(III) state due to incomplete conversion is marked by (#); a resonator background signal is marked by an asterisk (*). (c) Stack plot of CW X-band EPR spectra recorded from samples undergoing different aging times $t_a$. (d) Fraction of the *apo* and *holo* state as a function of $t_a$. The fractions have been derived from the signal amplitudes of *hs* Fe(III) and *ls* Fe(III) in the CW EPR spectra (SI Section 4.5) and are given as mean (full circle) ± SD (error bars) of triplicates. Solid lines: fit using two exponentials ($y = ae^{-k_1't} + be^{-k_2't}$) to experimental data. To ascertain pseudo-first-order kinetics, $NaN_3$ was used in 1000-fold excess. Postmixing concentrations: [MetMb] = 0.75 mM, [$NaN_3$] = 0.75 M. Note that at $t_a = 0$, about 5% *ls* Fe(III) MetMb is present.

using difference-distance maps generated with the *in-silico* spin-labeling program mtsslWizard (SI Section 5 and Figure S6).[58] The selection was based on three criteria: (1) one labeling site is on the $C_\alpha$-helix; (2) the distance distributions of *apo* and *holo* states range between 2 and 8 nm to facilitate high-quality PELDOR data; and (3) the distance distributions should be narrow (<1 nm full width at half-height, fwhh) and well separated ($\Delta r$ > 0.6 nm) to facilitate the identification of distance changes. The amino-acid pair E289R1/I340R1 (where R1 refers to the nitroxide-labeled cysteine) was particularly promising due to its large $\Delta r$ of −1.8 nm and its narrow distribution widths. In addition, the pair R254R1/E336R1 with a $\Delta r$ of only −0.3 nm was selected to gauge the limitations of the method.

**Controls.** We subjected these constructs to several controls to assess whether the spin label and the EPR sample preparation significantly affect the protein structure, the ligand binding, or the conformational change. First, we studied whether two native cysteine residues (C263, C331) of the CNBD were accessible for cysteine-reactive reagents and would interfere with distance determinations between exogenous spin labels. In the *apo* state, incubation of wild-type (wt) CNBD with Ellman's reagent modified approximately one cysteine per CNBD monomer, and the resulting protein was no longer able to bind cAMP. Therefore, we decided to remove the endogenous cysteines by site-directed mutagenesis. Of the different constructs, C263S/C331L, which was suggested by the software CUPSAT (Cologne University Protein Stability Analysis Tool),[59] displayed the lowest $K_D$ value for 8-(2-[7-nitro-4-benzofurazanyl]aminoethylthio)-adenosine-3′,5′-cyclic monophosphate (8-NBD-cAMP) (103 ± 27 mM). All mutants studied here are based on this cysteine-free C263S/C331L mutant.

Second, as spin labeling in high yields and quantitative cAMP removal required unfolding and refolding of the protein, we assessed the potential impact of unfolding/refolding on the distance distribution by also purifying and labeling the CNBD without unfolding (SI Section 2.8). The most probable distances and distribution widths of the *apo* and *holo* state of construct E289R1/I340R1 prepared via unfolding/refolding or in the native state agree well (Figure S8). Moreover, CW EPR spectra recorded at room temperature suggest that the local flexibility of the spin labels is similar for the two protein samples (Figure S9). This result indicates that the protein structure is not altered by unfolding and refolding.

Third, we probed how the R1 side chain affects binding of cAMP and 8-NBD-cAMP to the CNBD by independent techniques: the dissociation constants $K_D$ were determined either in a stopped-flow setup using the NBD fluorescence or by isothermal calorimetry (SI Section 3). Although the $K_D$ constants were altered, values were <10 $\mu$M, similar to the binding constants of cAMP and cGMP for the CNG channels in olfactory neurons and photoreceptors, respectively[5] (Table S5).

Fourth, we tested whether the structures of the *apo* and *holo* states are preserved upon labeling and freezing in the MHQ by comparing the experimental (PELDOR) distance distributions of the *apo* and *holo* states with those predicted by mtsslWizard or MMM on the basis of the NMR structures.[51] We have chosen the NMR structures instead of the crystal structures because crystal packing effects may have altered the structure and some of the amino-acid residues are not resolved in the crystal structure. The experimental distance distributions of the mutated and labeled CNBD are highly similar compared to the distance distributions generated *in silico* by means of mtsslWizard or MMM from the NMR structures of the native CNBD (Table S4). This comparison shows that the global protein structure has not been disturbed significantly.

Fifth, we compared the distance distributions of samples that were rapidly quenched in the MHQ ($t_a$ = 82 $\mu$s) with samples slowly immersed in liquid nitrogen (freezing time ~1.5 s).[37] Rapid freezing by MHQ does not allow for sufficient time to relax to the thermodynamic energy minimum at the freezing point, and, compared to slow freezing, a broader conformational ensemble may be trapped. This can lead to differences in the shape and width of the distance distributions depending on the freezing conditions.[37,38] Here, we find that distributions


https://doi.org/10.1021/jacs.1c01081
J. Am. Chem. Soc. 2021, 143, 6981−6989

broaden in fast-frozen samples, apart from the *apo* state of E289R1/I340R1, where the intensity ratios of the peaks at 4 nm are altered (Figure S10).

Finally, we examined whether the addition of 20% deuterated ethylene glycol (EG-$d_6$) as cryoprotectant affects the EPR properties of the spin system. We observed that the phase-memory time $T_M$ of the spin label increases from 2.5 to 3.2 $\mu$s upon adding EG-$d_6$, which enables longer time windows for the dipolar evolution in the PELDOR experiment and improves the signal-to-noise ratio[12] (Figure S11 and Table S6). In addition, the background correction of PELDOR time traces is improved, and thus more reliable distance distributions are obtained. Beyond this, the distance distributions with and without EG-$d_6$ are very similar, from which we conclude that the protein structure is not affected by the cryoprotectant.

In conclusion, these controls show that the label and rapid MHQ freezing does not alter the global structure or the function of the protein.

**Assessing the Conformational Change.** The *apo* state sample of the MloK1 CNBD was mixed in the MHQ with buffer only. The *holo* state, which is the cAMP/CNBD complex, was first formed outside of the MHQ by adding cAMP and then mixed with buffer in the MHQ. The final protein and cAMP concentrations after 1:1 mixing at $t_a$ = 82 $\mu$s were 150 $\mu$M and 15 mM, respectively. The background-corrected time traces and the corresponding distance distributions are shown in Figure 3 (SI Section 9.2).

The *apo* and *holo* state of E289R1/I340R1 display a bimodal distance distribution with both modes falling within the envelope predicted by mtsslWizard (Figure 3). We reason that the bimodality is caused by interactions of the label rotamers with the protein, which are difficult to predict by *in-silico* methods[60] (Figure S7). The change in the most probable distances, $\Delta r$ = −1.9 nm, between *apo* and *holo* state agrees with the mtsslWizard prediction. For the R254R1/E336R1 construct, experimental and predicted distance distributions for the *apo* and *holo* state also match within the error margin of mtsslWizard (0.4 nm). Based on the PELDOR background validation (Figure 3), the peak for the *apo* state at 2.5 and 2.8 nm for constructs E289R1/I340R1 and R254R1/E336R1, respectively, may indicate a small contribution of the *holo* state, whereas the minor peaks at longer distances are artifacts. Overall, the distance change of $\Delta r$ = −0.4 nm between the *apo* and *holo* state of R254R1/E336R1 is in good agreement with the mtsslWizard prediction. Due to the particularly small distance change and large overlap between the distance distributions of *apo* and *holo*, this construct indeed illustrates the resolution of our method.

Next, we examined the kinetics of the conformational change during the transition from the *apo* to the *holo* state by varying $t_a$ from 82 to 498 $\mu$s. After 1:1 mixing the protein sample (200 $\mu$L) in the MHQ with cAMP-containing buffer (500 $\mu$L), final protein and cAMP concentrations were 150 $\mu$M and 15 mM, respectively. Of note, the mixer had been first conditioned with an excess of cAMP-containing buffer (300 $\mu$L) before the *apo* protein entered the mixer. This precaution ascertains that the protein sample was not partially mixed with buffer that did not contain cAMP.

As can be gleaned from Figure 4a,d, the time traces and the distance distributions change with $t_a$. The time-resolved changes in the distance distributions for E289R1/I340R1 show that with increasing $t_a$, the *apo* and *holo* state populations

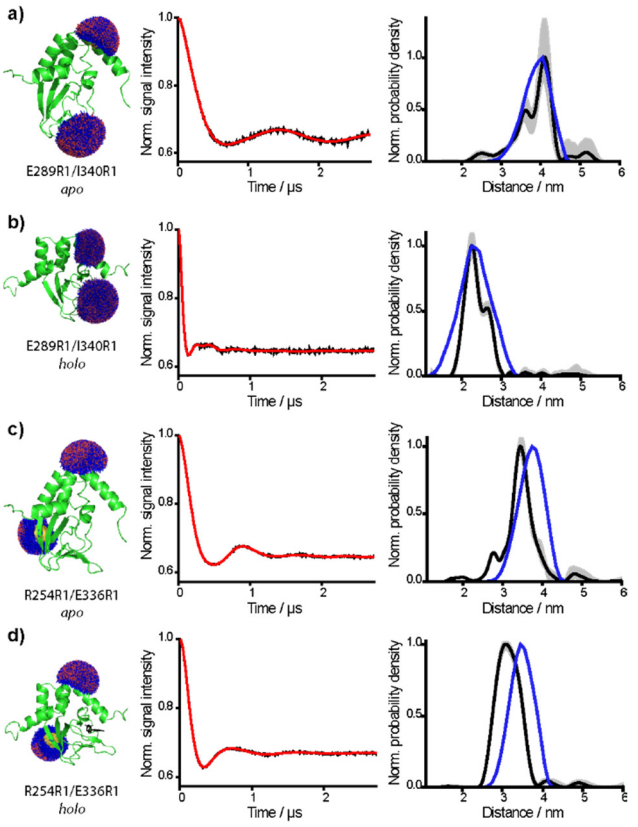


**Figure 3.** PELDOR data for *apo* and *holo* states of E289R1/I340R1 and R254R1/E336R1. Rotamer distribution of R1 (blue) based on the NMR structure (green) (PDB IDs: 2kxl, *apo* and 2k0g, *holo*) (left panels). Background-corrected time traces (black lines) for the *apo* and *holo* state and the respective fits (red lines) (middle panels). Distance distributions of the *apo* and *holo* state corresponding to the respective time traces in middle panels. The *y*-axis is normalized to the maximum of the probability density of the best fit (black line). Background validation is shown as gray-shaded areas. The distance distributions predicted by mtsslWizard are shown as blue lines (right panels). (a) E289R1/I340R1 *apo* state. (b) E289R1/I340R1 *holo* state. (c) R254R1/E336R1 *apo* state. (d) R254R1/E336R1 *holo* state. Both, the *apo* and *holo* samples of R254R1/E336R1 and E289R1/I340R1 were prepared at MHQ aging times $t_a$ of 82 $\mu$s. For the *apo* state, the postmixing concentration was [CNBD] = 150 $\mu$M. The *holo* form was produced by adding cAMP to the *apo* form outside the MHQ, before mixing with buffer in the MHQ, yielding final concentrations of [CNBD] = 150 $\mu$M and [cAMP] = 15 mM.

respectively decreased and increased stoichiometrically (Figure 4b,c and Extended Data Figure 2, SI Section 9.2). However, neither a gradual shift of the most probable distance from the *apo* to the *holo* state nor additional peaks along the reaction coordinate were observed, suggesting that structural intermediates are not detected.

The fraction of *apo* and *holo* state was quantified by deconvolution of the PELDOR time traces (SI Section 4.7). A plot of the fractions of *apo* and *holo* state versus $t_a$ was fitted by a monoexponential function:

$$y = y_0 + A\, e^{-kt}$$

yielding a rate constant $k$ of 7398 ± 1179 $s^{-1}$ for E289R1/I340R1 and of 7508 ± 867 $s^{-1}$ for R254R1/E336R1. All regression parameters are collected in Table S3. Interestingly, the $k$ values are highly similar, indicating that the underlying


https://doi.org/10.1021/jacs.1c01081
J. Am. Chem. Soc. 2021, 143, 6981−6989

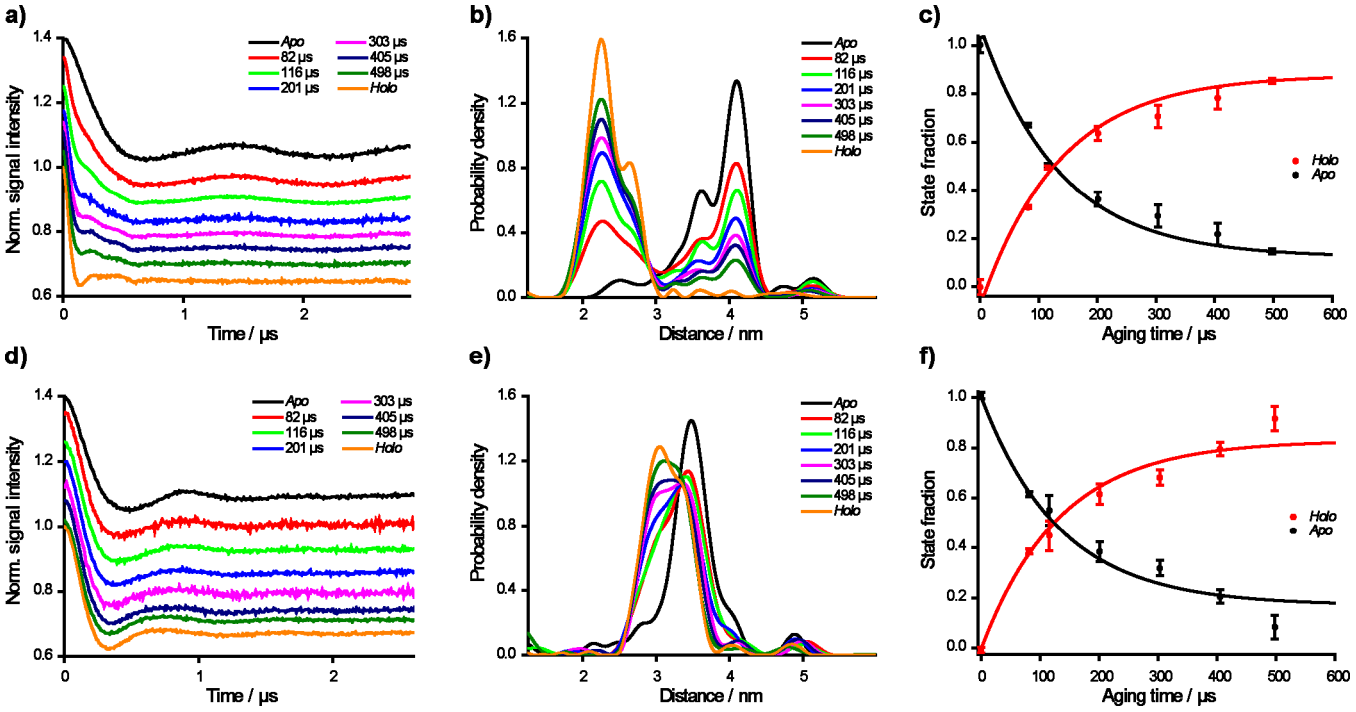


**Figure 4.** Time-resolved PELDOR data. The background-corrected PELDOR time traces obtained for aging times $t_a$ ranging from 82 to 498 $\mu$s (color code see legend) for (a) E289R1/I340R1 and (d) R254R1/E336R1. Note that the time traces were normalized but shifted on the *y*-axis for the sake of clarity. The postmixing concentrations were [CNBD] = 150 $\mu$M and [cAMP] = 15 mM, respectively. The corresponding distance distributions are shown in (b) for E289R1/I340R1 and in (e) for R254R1/E336R1. In (c) and (f), the fractions of *apo* and *holo* state are plotted against $t_a$. Data points represent the mean; the error bars, the standard deviation ($n$ = 3 experiments). Data have been fitted with a monoexponential function, indicated by red and black lines (R289R1/I340R1: $R^2$ = 0.982; R254R1/E336R1: $R^2$ = 0.993).

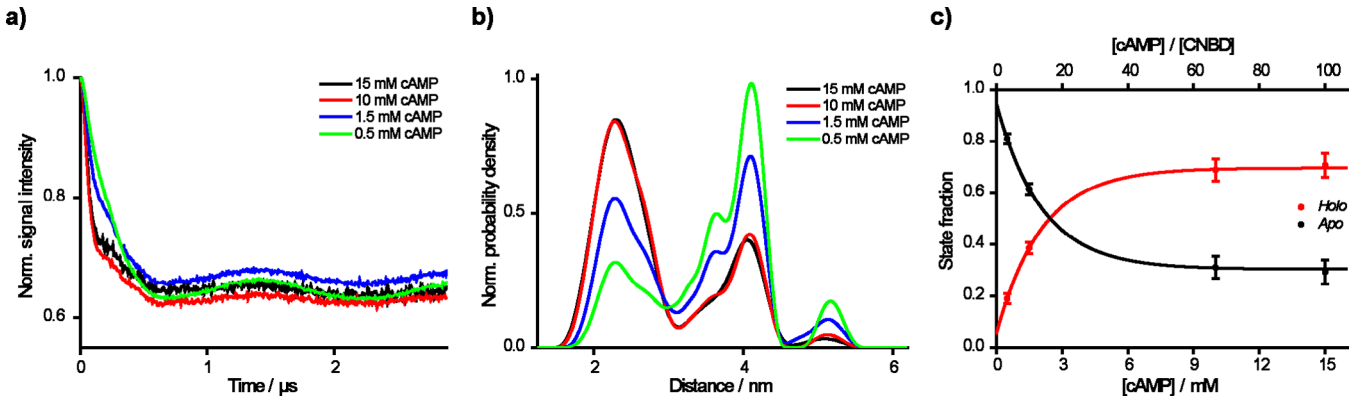


**Figure 5.** cAMP concentration series for E289R1/I340R1 at $t_a$ = 303 $\mu$s. (a) Background-corrected PELDOR time traces for final [cAMP] = 0.5 mM (green), 1.5 mM (blue), 10 mM (red), and 15 mM (black). (b) Corresponding distance distributions using the same color code as in (a). (c) Plot of the fractions of *apo* and *holo* state against cAMP concentration. Data represent the mean ± SD ($n$ = 3 experiments).

process monitored by MHQ/PELDOR is independent of the labeling site on the $C_\alpha$-helix. In addition, construct R254R1/E336R1 illustrates that even changes as small as 0.4 nm of strongly overlapping distance distributions can be resolved.

Because our experiments monitor ensemble averages, the $C_\alpha$-helix movement of individual molecules, which supposedly is rapid and stochastic, is not resolved in the MHQ/PELDOR experiment. Indeed, molecular dynamics (MD) simulation suggests that the helix movement takes only a few nanoseconds, which is much faster than the experimental rate constant $k$ (Figure S13 and Extended Data Figure 5, SI Section 9.3). Therefore, we scrutinized whether the kinetics reflects rate-limiting cAMP binding. To this end, MHQ samples were prepared at a $t_a$ of 303 $\mu$s. The protein concentration after 1:1 mixing in the MHQ was in each case 150 $\mu$M, whereas the final cAMP concentration varied between 0.5 and 15 mM, equivalent to a CNBD/cAMP ratio ranging from 1:3 to 1:100. The background-corrected PELDOR time traces, the corresponding distance distributions, and the calculated fraction of *apo* and *holo* state versus cAMP concentration are shown in Figure 5 (Extended Data Figure 3, SI Section 9.2).

At cAMP concentrations larger than 10 mM ([cAMP]/[CNBD] ~67), the fractions are independent of the cAMP concentration, confirming saturation of the CNBD with cAMP. This demonstrates that diffusion-controlled ligand binding under the MHQ/PELDOR conditions is not rate-limiting and that the rate-limiting step occurs further down the *apo*-to-*holo* pathway. This conclusion was confirmed by measuring the


https://doi.org/10.1021/jacs.1c01081
J. Am. Chem. Soc. 2021, 143, 6981−6989

ligand-binding kinetics in a stopped-flow device using fluorescence spectroscopy (Table S5).

## DISCUSSION

Here we combined PELDOR with the rapid-freezing technique MHQ to follow changes in protein conformation on a time scale of >82 $\mu$s with high precision. Labels at two different sites in the $C_\alpha$-helix of a CNBD report distance changes of 0.4 and 1.9 nm, respectively, yet the rate constants for the conformational change are virtually identical. In addition, amino acids E336 and I340 are only three residues apart, yet display very different $\Delta r$ values. For a linear movement around the hinge between $B_\alpha$ and $C_\alpha$ (Figure 1), a similar $\Delta r$ is expected for both residues. Our data thus suggest that upon ligand binding, $C_\alpha$ not only moves closer to the $\beta$-sheet domain but also rotates, which is also observed in the NMR structures. Finally, the data set for R254R1/E336R1 illustrates the strength of the MHQ/PELDOR combination for monitoring local conformational changes in proteins, even if the distance changes are as small as 0.4 nm.

We observed a gradual transition from the *apo* to the *holo* state, but detected no distinct population that would indicate a conformational intermediate (Figure 4). This result can be interpreted in light of the concept of dwell or waiting times.[61] In this concept, ligand binding and conformational change are both thermally driven processes. A free-energy profile for a simplified case involves only three distinct states: (1) the protein in the *apo* state plus unbound ligand; (2) the ligand complexed to the protein, but the protein still being in the *apo* state; and (3) the ligand bound to the protein in the final *holo* structure (Figure 6).

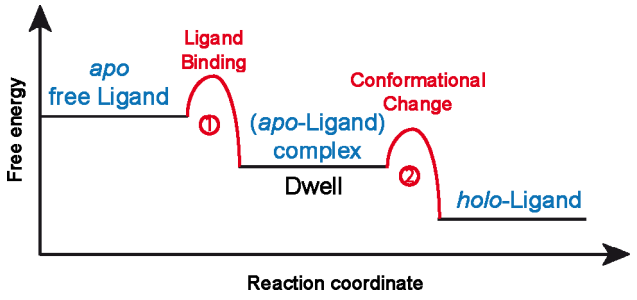


**Figure 6.** Schematic free-energy profile of a ligand-induced conformational change in a protein. The transition events are marked in red. The length of the dwell time is individual for every individual molecule. Depending on the spectroscopic technique used, i.e., whether the ligand or the protein is observed, the method will report on different states of this landscape (see text).

The crossings of the two free-energy barriers, that is, the complexation of ligand to the *apo* structure and the subsequent conformational transition to the final *holo* structure, both occur in the nanosecond to low microsecond range. Thus, they exceed the time resolution of the MHQ device (<80 $\mu$s). However, the dwell time of the system in the ligand-complexed *apo* state can be considerably longer, spanning the range from a few to hundreds of microseconds. Thus, binding at high ligand concentrations and conformational transition happen on time scales that are largely different from the dwell time of the *apo*-ligand complex. At lower ligand concentrations, the binding event becomes rate limiting (Figure 5).

The dwell time of the *apo*-ligand complex is different for each individual protein molecule, resulting macroscopically in a distribution of dwell times. Such a distribution of dwell times is also compatible with MD simulations, which show that dwell times of the *apo*-ligand complex derived from MD trajectories are exponentially distributed (Figure S14 and SI Section 9.3). For short aging times $t_a$ in relation to the individual dwell time, only a small number of protein molecules can undergo the conformational transition. For longer aging times, the probability increases that protein molecules populate the *holo* state. Thus, the time constants determined for E289R1/I340R1 and R254R1/E336R1 reflect the average dwell times for the cAMP-induced conformational change rather than the $C_\alpha$-helix movement or the binding kinetics themselves. This picture agrees with recent atomistic simulations, which revealed "prebinding" of the ligand to different surface sites, followed by induced-fit conformational motions of the binding pocket and entropic barriers to ligand binding as the rate-limiting steps.[52] We note that this concept neither rules out conformational motions during the first ligand binding steps that, however, are below the PELDOR resolution, nor claims that, for the *apo*-ligand complex, the ligand is already positioned at its final binding site. It does imply, though, that the second step is independent of concentration. Thus, MHQ/PELDOR is able to extract dwell times from conformational rearrangements, further illustrating the power of this technique to study ligand-triggered protein kinetics. Comparing the PELDOR-derived dwell times with those inferred from MD reveals an 18-fold difference (Figure S14). This discrepancy may be attributed to two factors. First, the temperature of the solution jet is not precisely known, but likely below room temperature, and may decrease gradually over the jet length. By contrast, the MD simulation temperature was 300 K. Thus, the experimentally determined dwell times are expected to be longer. Second, because the entire conformational change is a stochastic multistage process whose duration exceeds the simulation time of 3.5 $\mu$s, only the first step(s) en route to the *holo* state is monitored in the MD simulation. Thus, the MD simulation probably underestimates the overall dwell time. This combination of overestimation of dwell times in the experiment and underestimation in the MD simulation may explain the discrepancy.

For this proof-of-concept study, we used high concentrations and larger volumes to obtain high-quality data at short measurement times (60 nmol protein, 200 $\mu$L, i.e., 300 $\mu$M per time point at a signal-to-noise ratio (SNR) between 70 and 100 $h^{-1/2}$ and a time trace length of 2.8 $\mu$s). To demonstrate the sensitivity of MHQ/PELDOR, we also used protein amounts as small as 7.5 nmol (75 $\mu$M, 100 $\mu$L) per time point, which still yielded a good SNR of 25 for a measurement time of 8 h (SI Section 8). Thus, the protein amount, measurement time, and SNR can be similar to that of typical Q-band PELDOR measurements. Sample consumption can be reduced even further when working at higher EPR frequencies such as W-band.[40,62]

Spatiotemporal resolution has also been achieved with other methods, each having its own strengths and limitations and often being complementary to each other. For example, a fluorescently labeled ligand, such as 8-NBD-cAMP,[63,64] versus a spin label addresses two different observables: fluorescence spectroscopy probes the environment of the cAMP ligand and thus reports on the crossing of barrier 1 in Figure 6 (aqueous solution vs complexation in the hydrophobic protein), whereas


https://doi.org/10.1021/jacs.1c01081
J. Am. Chem. Soc. 2021, 143, 6981−6989

PELDOR reports on the *apo*-to-*holo* transition, which is rate-limited by the dwell time of the ligand-complexed *apo* state. A further example is time-resolved Förster resonance energy transfer (trFRET). It is measured in solution at ambient temperatures,[65] whereas MHQ/PELDOR is measured in the frozen state. Yet, MHQ/PELDOR has the advantages that (1) the two sites carry the same label, and orthogonal labeling with two different labels as in FRET is obsolete; (2) due to the small size of spin labels, the alteration of the native protein structure is likely less severe and distance measurements are more precise; (3) the circumvention of the $\kappa^2$-problem by measuring the whole Pake pattern makes the data analysis parameter-free; and (4) the accessible distance range is larger than for a single FRET pair.[66] Another example is time-resolved solution NMR at room temperature.[67] NMR spectroscopy, like MHQ/PELDOR, requires substantial amounts of protein sample, yet MHQ/PELDOR has no limitation with respect to the size of the biomolecule.

## CONCLUSION

In conclusion, the MHQ/PELDOR approach holds great potential for following conformational changes in large biomolecules with spatiotemporal resolution on the angstrom and microsecond time scale. In our proof-of-concept study, we have determined the mean dwell time for a helix movement triggered by a small ligand. MHQ/PELDOR holds promise to temporally resolve both dwell times and slower conformational transitions that happen in the >100 $\mu$s range. On a final note, MHQ/PELDOR is by no means restricted to proteins: It might be useful to follow conformational changes in any biomolecule, provided that these changes can be triggered by an external event such as ligand binding and that they proceed on a time scale of >82 $\mu$s. As the MHQ device is operated under a vacuum hood, quick changes of pressure or temperature are presumably difficult to implement. However, we envision to use the MHQ as a fast-freezing device and trigger folding events or conformational changes by light using photolysis of caged compounds, photoswitches, or photo-triggers.

## ASSOCIATED CONTENT

### Supporting Information

The Supporting Information is available free of charge at https://pubs.acs.org/doi/10.1021/jacs.1c01081.

Instrumentation, detailed experimental procedures (protein preparation, EPR sample preparation), details on data analysis, details on MD simulations (PDF)

## AUTHOR INFORMATION


### Corresponding Authors

**Olav Schiemann** − *Institute of Physical and Theoretical Chemistry, University of Bonn, 53115 Bonn, Germany;* orcid.org/0000-0001-6346-9779; Email: schiemann@pc.uni-bonn.de

**U. Benjamin Kaupp** − *Center of Advanced European Studies and Research (caesar), 53175 Bonn, Germany; Life & Medical Sciences Institute (LIMES), University of Bonn, 53115 Bonn, Germany;* orcid.org/0000-0002-0696-6397; Email: u.b.kaupp@caesar.de

### Authors

**Tobias Hett** − *Institute of Physical and Theoretical Chemistry, University of Bonn, 53115 Bonn, Germany;* orcid.org/0000-0003-3821-5165

**Tobias Zbik** − *Center of Advanced European Studies and Research (caesar), 53175 Bonn, Germany*

**Shatanik Mukherjee** − *Center of Advanced European Studies and Research (caesar), 53175 Bonn, Germany*

**Hideto Matsuoka** − *Institute of Physical and Theoretical Chemistry, University of Bonn, 53115 Bonn, Germany;* Present Address: H.M.: Graduate School of Science, Osaka City University, 3-3-138 Sugimoto, Sumiyoshi-ku, Osaka, 558-8585, Japan.

**Wolfgang Bönigk** − *Center of Advanced European Studies and Research (caesar), 53175 Bonn, Germany*

**Daniel Klose** − *Fachbereich Physik, Universität Osnabrück, 49076 Osnabrück, Germany;* Present Address: D.K.: Departement Chemie and Angewandte Biowissenschaften, Lab. Für Physikalische Chemie, ETH Zürich, Vladimir-Prelog-Weg 1-5/10, 8093 Zürich, Switzerland.; orcid.org/0000-0002-3597-0889

**Christophe Rouillon** − *Center of Advanced European Studies and Research (caesar), 53175 Bonn, Germany*

**Norbert Brenner** − *Center of Advanced European Studies and Research (caesar), 53175 Bonn, Germany*

**Sebastian Peuker** − *Center of Advanced European Studies and Research (caesar), 53175 Bonn, Germany*

**Reinhard Klement** − *Department of Theoretical and Computational Biophysics, Max Planck Institute for Biophysical Chemistry, 37077 Göttingen, Germany*

**Heinz-Jürgen Steinhoff** − *Fachbereich Physik, Universität Osnabrück, 49076 Osnabrück, Germany*

**Helmut Grubmüller** − *Department of Theoretical and Computational Biophysics, Max Planck Institute for Biophysical Chemistry, 37077 Göttingen, Germany;* orcid.org/0000-0002-3270-3144

**Reinhard Seifert** − *Center of Advanced European Studies and Research (caesar), 53175 Bonn, Germany*

Complete contact information is available at: https://pubs.acs.org/10.1021/jacs.1c01081

### Author Contributions

‡T.H. and T.Z. contributed equally.


### Notes

The authors declare no competing financial interest.

## ACKNOWLEDGMENTS

Funding by the DFG via a Reinhart Koselleck Grant (Projektnummer 420322655) to U.B.K. and the University of Bonn via TRA-2 (Building Blocks of Matter and Fundamental Interactions) is gratefully acknowledged.

## REFERENCES

(1) Hilger, D.; Masureel, M.; Kobilka, B. K. Structure and dynamics of GPCR signaling complexes. *Nat. Struct. Mol. Biol.* **2018**, *25* (1), 4−12.

(2) Rosenbaum, D. M.; Rasmussen, S. G. F.; Kobilka, B. K. The structure and function of G-protein-coupled receptors. *Nature* **2009**, *459* (7245), 356−363.

(3) Kaupp, U. B. Olfactory signalling in vertebrates and insects: differences and commonalities. *Nat. Rev. Neurosci.* **2010**, *11* (3), 188−200.

(4) Kaupp, U. B.; Seifert, R. Molecular Diversity of Pacemaker Ion Channels. *Annu. Rev. Physiol.* **2001**, *63* (1), 235−257.
(5) Kaupp, U. B.; Seifert, R. Cyclic Nucleotide-Gated Ion Channels. *Physiol. Rev.* **2002**, *82* (3), 769−824.
(6) Weis, W. I.; Kobilka, B. K. The Molecular Basis of G Protein-Coupled Receptor Activation. *Annu. Rev. Biochem.* **2018**, *87* (1), 897−919.
(7) Bezanilla, F. How membrane proteins sense voltage. *Nat. Rev. Mol. Cell Biol.* **2008**, *9* (4), 323−332.
(8) Hofmann, K. P.; Scheerer, P.; Hildebrand, P. W.; Choe, H.-W.; Park, J. H.; Heck, M.; Ernst, O. P. A G protein-coupled receptor at work: the rhodopsin model. *Trends Biochem. Sci.* **2009**, *34* (11), 540−552.
(9) Sattig, T.; Rickert, C.; Bamberg, E.; Steinhoff, H.-J.; Bamann, C. Light-Induced Movement of the Transmembrane Helix B in Channelrhodopsin-2. *Angew. Chem., Int. Ed.* **2013**, *52* (37), 9705−9708.
(10) Jin, P.; Jan, L. Y.; Jan, Y.-N. Mechanosensitive Ion Channels: Structural Features Relevant to Mechanotransduction Mechanisms. *Annu. Rev. Neurosci.* **2020**, *43* (1), 207−229.
(11) Klostermeier, D.; Rudolph, M. G. *Biophysical Chemistry*; CRC Press, 2017.
(12) Jeschke, G. DEER Distance Measurements on Proteins. *Annu. Rev. Phys. Chem.* **2012**, *63* (1), 419−446.
(13) Milov, A. D.; Salikhov, K. M.; Schirov, M. D. Application of ELDOR in electron-spin echo for paramagnetic center space distribution in solids. *Fiz. Tverd. Tela (Leningrad)* **1981**, *23*, 975−982.
(14) Pannier, M.; Veit, S.; Godt, A.; Jeschke, G.; Spiess, H. Dead-Time Free Measurement of Dipole-Dipole Interactions between Electron Spins. *J. Magn. Reson.* **2000**, *142* (2), 331−340.
(15) Schmidt, T.; Wälti, M. A.; Baber, J. L.; Hustedt, E. J.; Clore, G. M. Long Distance Measurements up to 160 Å in the GroEL Tetradecamer Using Q-Band DEER EPR Spectroscopy. *Angew. Chem., Int. Ed.* **2016**, *55* (51), 15905−15909.
(16) Timmel, C. R.; Harmer, J. R., Eds. *Structural Information from Spin-Labels and Intrinsic Paramagnetic Centres in the Biosciences*; Structure and Bonding, Vol. *152*; Springer: Berlin Heidelberg, 2013; DOI: 10.1007/978-3-642-39125-5.
(17) Hagelueken, G.; Ingledew, W. J.; Huang, H.; Petrovic-Stojanovska, B.; Whitfield, C.; ElMkami, H.; Schiemann, O.; Naismith, J. H. PELDOR Spectroscopy Distance Fingerprinting of the Octameric Outer-Membrane Protein Wza from Escherichia coli. *Angew. Chem., Int. Ed.* **2009**, *48* (16), 2904−2906.
(18) Pliotas, C.; Ward, R.; Branigan, E.; Rasmussen, A.; Hagelueken, G.; Huang, H.; Black, S. S.; Booth, I. R.; Schiemann, O.; Naismith, J. H. Conformational state of the MscS mechanosensitive channel in solution revealed by pulsed electron-electron double resonance (PELDOR) spectroscopy. *Proc. Natl. Acad. Sci. U. S. A.* **2012**, *109* (40), E2675−E2682.
(19) Halbmair, K.; Seikowski, J.; Tkach, I.; Höbartner, C.; Sezer, D.; Bennati, M. High-resolution measurement of long-range distances in RNA: pulse EPR spectroscopy with TEMPO-labeled nucleotides. *Chemical Science* **2016**, *7* (5), 3172−3180.
(20) Heinz, M.; Erlenbach, N.; Stelzl, L. S.; Thierolf, G.; Kamble, N. R.; Sigurdsson, S. T.; Prisner, T. F.; Hummer, G. High-resolution EPR distance measurements on RNA and DNA with the non-covalent G spin label. *Nucleic Acids Res.* **2020**, *48* (2), 924−933.
(21) Wuebben, C.; Vicino, M. F.; Mueller, M.; Schiemann, O. Do the P1 and P2 hairpins of the Guanidine-II riboswitch interact? *Nucleic Acids Res.* **2020**, *48* (18), 10518−10526.
(22) Constantinescu-Aruxandei, D.; Petrovic-Stojanovska, B.; Schiemann, O.; Naismith, J. H.; White, M. F. Taking a molecular motor for a spin: helicase mechanism studied by spin labeling and PELDOR. *Nucleic Acids Res.* **2016**, *44* (2), 954−968.
(23) Duss, O.; Michel, E.; Yulikov, M.; Schubert, M.; Jeschke, G.; Allain, F. H.-T. Structural basis of the non-coding RNA RsmZ acting as a protein sponge. *Nature* **2014**, *509* (7502), 588−592.
(24) Duss, O.; Yulikov, M.; Jeschke, G.; Allain, F. H.-T. EPR-aided approach for solution structure determination of large RNAs or protein-RNA complexes. *Nat. Commun.* **2014**, *5* (1), 3669.
(25) Vazquez Reyes, C.; Tangprasertchai, N. S.; Yogesha, S. D.; Nguyen, R. H.; Zhang, X.; Rajan, R.; Qin, P. Z. Nucleic Acid-Dependent Conformational Changes in CRISPR-Cas9 Revealed by Site-Directed Spin Labeling. *Cell Biochem. Biophys.* **2017**, *75* (2), 203−210.
(26) Wu, Z.; Feintuch, A.; Collauto, A.; Adams, L. A.; Aurelio, L.; Graham, B.; Otting, G.; Goldfarb, D. Selective Distance Measurements Using Triple Spin Labeling with $Gd^{3+}$, $Mn^{2+}$, and a Nitroxide. *J. Phys. Chem. Lett.* **2017**, *8* (21), 5277−5282.
(27) Borbat, P. P.; Mchaourab, H. S.; Freed, J. H. Protein Structure Determination Using Long-Distance Constraints from Double-Quantum Coherence ESR: Study of T4 Lysozyme. *J. Am. Chem. Soc.* **2002**, *124* (19), 5304−5314.
(28) Yang, Z.; Liu, Y.; Borbat, P.; Zweier, J. L.; Freed, J. H.; Hubbell, W. L. Pulsed ESR Dipolar Spectroscopy for Distance Measurements in Immobilized Spin Labeled Proteins in Liquid Solution. *J. Am. Chem. Soc.* **2012**, *134* (24), 9950−9952.
(29) Bleicken, S.; Jeschke, G.; Stegmueller, C.; Salvador-Gallego, R.; García-Sáez, A. J.; Bordignon, E. Structural Model of Active Bax at the Membrane. *Mol. Cell* **2014**, *56* (4), 496−505.
(30) Galazzo, L.; Meier, G.; Timachi, M. H.; Hutter, C. A. J.; Seeger, M. A.; Bordignon, E. Spin-labeled nanobodies as protein conformational reporters for electron paramagnetic resonance in cellular membranes. *Proc. Natl. Acad. Sci. U. S. A.* **2020**, *117* (5), 2441−2448.
(31) Joseph, B.; Sikora, A.; Bordignon, E.; Jeschke, G.; Cafiso, D. S.; Prisner, T. F. Distance Measurement on an Endogenous Membrane Transporter in E. coli Cells and Native Membranes Using EPR Spectroscopy. *Angew. Chem., Int. Ed.* **2015**, *54* (21), 6196−6199.
(32) Ward, R.; Pliotas, C.; Branigan, E.; Hacker, C.; Rasmussen, A.; Hagelueken, G.; Booth, I. R.; Miller, S.; Lucocq, J.; Naismith, J. H.; Schiemann, O. Probing the Structure of the Mechanosensitive Channel of Small Conductance in Lipid Bilayers with Pulsed Electron-Electron Double Resonance. *Biophys. J.* **2014**, *106* (4), 834−842.
(33) Fleck, N.; Heubach, C. A.; Hett, T.; Haege, F. R.; Bawol, P. P.; Baltruschat, H.; Schiemann, O. SLIM: A Short-Linked, Highly Redox-Stable Trityl Label for High-Sensitivity In-Cell EPR Distance Measurements. *Angew. Chem., Int. Ed.* **2020**, *59* (24), 9767−9772.
(34) Krstić, I.; Hänsel, R.; Romainczyk, O.; Engels, J. W.; Dötsch, V.; Prisner, T. F. Long-Range Distance Measurements on Nucleic Acids in Cells by Pulsed EPR Spectroscopy. *Angew. Chem., Int. Ed.* **2011**, *50* (22), 5070−5074.
(35) Qi, M.; Groß, A.; Jeschke, G.; Godt, A.; Drescher, M. Gd(III)-PyMTA Label Is Suitable for In-Cell EPR. *J. Am. Chem. Soc.* **2014**, *136* (43), 15366−15378.
(36) Yang, Y.; Pan, B.-B.; Tan, X.; Yang, F.; Liu, Y.; Su, X.-C.; Goldfarb, D. In-Cell Trityl-Trityl Distance Measurements on Proteins. *J. Phys. Chem. Lett.* **2020**, *11* (3), 1141−1147.
(37) Georgieva, E. R.; Roy, A. S.; Grigoryants, V. M.; Borbat, P. P.; Earle, K. A.; Scholes, C. P.; Freed, J. H. Effect of freezing conditions on distances and their distributions derived from Double Electron Electron Resonance (DEER): A study of doubly-spin-labeled T4 lysozyme. *J. Magn. Reson.* **2012**, *216*, 69−77.
(38) Schmidt, T.; Jeon, J.; Okuno, Y.; Chiliveri, S. C.; Clore, G. M. Submillisecond Freezing Permits Cryoprotectant-Free EPR Double Electron-Electron Resonance Spectroscopy. *ChemPhysChem* **2020**, *21* (12), 1224−1229.
(39) Cherepanov, A. V.; de Vries, S. Microsecond freeze-hyper-quenching: development of a new ultrafast micro-mixing and sampling technology and application to enzyme catalysis. *Biochim. Biophys. Acta, Bioenerg.* **2004**, *1656* (1), 1−31.
(40) Collauto, A.; DeBerg, H. A.; Kaufmann, R.; Zagotta, W. N.; Stoll, S.; Goldfarb, D. Rates and equilibrium constants of the ligand-induced conformational transition of an HCN ion channel protein domain determined by DEER spectroscopy. *Phys. Chem. Chem. Phys.* **2017**, *19* (23), 15324−15334.

(41) Pievo, R.; Angerstein, B.; Fielding, A. J.; Koch, C.; Feussner, I.; Bennati, M. A Rapid Freeze-Quench Setup for Multi-Frequency EPR Spectroscopy of Enzymatic Reactions. *ChemPhysChem* **2013**, *14* (18), 4094−4101.
(42) de Vries, S. The role of the conserved tryptophan272 of the Paracoccus denitrificans cytochrome c oxidase in proton pumping. *Biochim. Biophys. Acta, Bioenerg.* **2008**, *1777* (7−8), 925−928.
(43) Paulus, A.; Werner, C.; Ludwig, B.; de Vries, S. The cytochrome ba3 oxidase from Thermus thermophilus does not generate a tryptophan radical during turnover: Implications for the mechanism of proton pumping. *Biochim. Biophys. Acta, Bioenerg.* **2015**, *1847* (10), 1093−1100.
(44) Wiertz, F. G. M.; Richter, O.-M. H.; Ludwig, B.; de Vries, S. Kinetic Resolution of a Tryptophan-radical Intermediate in the Reaction Cycle of Paracoccus denitrificans Cytochrome c Oxidase. *J. Biol. Chem.* **2007**, *282* (43), 31580−31591.
(45) Srour, B.; Strampraad, M. J.; Hagen, W. R.; Hagedoorn, P.-L. Refolding kinetics of cytochrome c studied with microsecond timescale continuous-flow UV-vis spectroscopy and rapid freeze-quench EPR. *J. Inorg. Biochem.* **2018**, *184*, 42−49.
(46) de Vries, S.; Dörner, K.; Strampraad, M. J. F.; Friedrich, T. Electron Tunneling Rates in Respiratory Complex I Are Tuned for Efficient Energy Conversion. *Angew. Chem., Int. Ed.* **2015**, *54* (9), 2844−2848.
(47) Kowal, J.; Biyani, N.; Chami, M.; Scherer, S.; Rzepiela, A. J.; Baumgartner, P.; Upadhyay, V.; Nimigean, C. M.; Stahlberg, H. High-Resolution Cryoelectron Microscopy Structure of the Cyclic Nucleotide-Modulated Potassium Channel MloK1 in a Lipid Bilayer. *Structure* **2018**, *26* (1), 20−27 e3.
(48) Nimigean, C. M.; Shane, T.; Miller, C. A Cyclic Nucleotide Modulated Prokaryotic $K^+$ Channel. *J. Gen. Physiol.* **2004**, *124* (3), 203−210.
(49) Clayton, G. M.; Silverman, W. R.; Heginbotham, L.; Morais-Cabral, J. H. Structural Basis of Ligand Activation in a Cyclic Nucleotide Regulated Potassium Channel. *Cell* **2004**, *119* (5), 615−627.
(50) Schünke, S.; Stoldt, M.; Novak, K.; Kaupp, U. B.; Willbold, D. Solution structure of the Mesorhizobium loti K1 channel cyclic nucleotide-binding domain in complex with cAMP. *EMBO Rep.* **2009**, *10* (7), 729−735.
(51) Schünke, S.; Stoldt, M.; Lecher, J.; Kaupp, U. B.; Willbold, D. Structural insights into conformational changes of a cyclic nucleotide-binding domain in solution from Mesorhizobium loti K1 channel. *Proc. Natl. Acad. Sci. U. S. A.* **2011**, *108* (15), 6121−6126.
(52) Voß, B.; Seifert, R.; Kaupp, U. B.; Grubmüller, H. A Quantitative Model for cAMP Binding to the Binding Domain of MloK1. *Biophys. J.* **2016**, *111* (8), 1668−1678.
(53) Puljung, M. C.; DeBerg, H. A.; Zagotta, W. N.; Stoll, S. Double electron-electron resonance reveals cAMP-induced conformational change in HCN channels. *Proc. Natl. Acad. Sci. U. S. A.* **2014**, *111* (27), 9816−9821.
(54) Evans, E. G. B.; Morgan, J. L. W.; DiMaio, F.; Zagotta, W. N.; Stoll, S. Allosteric conformational change of a cyclic nucleotide-gated ion channel revealed by DEER spectroscopy. *Proc. Natl. Acad. Sci. U. S. A.* **2020**, *117* (20), 10839−10847.
(55) Panarelli, E. G.; van der Meer, H.; Gast, P.; Groenen, E. J. J.; Blanco, F. J. Effective coupling of rapid freeze-quench to high-frequency electron paramagnetic resonance. *PLoS One* **2020**, *15* (5), No. e0232555.
(56) Fittipaldi, M.; García-Rubio, I.; Trandafir, F.; Gromov, I.; Schweiger, A.; Bouwen, A.; van Doorslaer, S. A Multi-Frequency Pulse EPR and ENDOR Approach to Study Strongly Coupled Nuclei in Frozen Solutions of High-Spin Ferric Heme Proteins. *J. Phys. Chem. B* **2008**, *112* (12), 3859−3870.
(57) Maurus, R.; Bogumil, R.; Nguyen, N. T.; Mauk, A. G.; Brayer, G. Structural and spectroscopic studies of azide complexes of horse heart myoglobin and the His-64→Thr variant. *Biochem. J.* **1998**, *332* (1), 67−74.
(58) Hagelueken, G.; Abdullin, D.; Schiemann, O. mtsslSuite. Probing Biomolecular Conformation by Spin-Labeling Studies. *Methods Enzymol.* **2015**, *563*, 595−622.
(59) Parthiban, V.; Gromiha, M. M.; Schomburg, D. CUPSAT: prediction of protein stability upon point mutations. *Nucleic Acids Res.* **2006**, *34*, W239−W242.
(60) Polyhach, Y.; Bordignon, E.; Jeschke, G. Rotamer libraries of spin labelled cysteines for protein studies. *Phys. Chem. Chem. Phys.* **2011**, *13* (6), 2356−2366.
(61) Weikl, T. R.; Paul, F. Conformational selection in protein binding and function. *Protein Sci.* **2014**, *23* (11), 1508−1518.
(62) Cruickshank, P. A. S.; Bolton, D. R.; Robertson, D. A.; Hunter, R. I.; Wylde, R. J.; Smith, G. M. A kilowatt pulsed 94 GHz electron paramagnetic resonance spectrometer with high concentration sensitivity, high instantaneous bandwidth, and low dead time. *Rev. Sci. Instrum.* **2009**, *80* (10), 103102.
(63) Cukkemane, A.; Grüter, B.; Novak, K.; Gensch, T.; Bönigk, W.; Gerharz, T.; Kaupp, U. B.; Seifert, R. Subunits act independently in a cyclic nucleotide-activated $K^+$ channel. *EMBO Rep.* **2007**, *8* (8), 749−755.
(64) Peuker, S.; Cukkemane, A.; Held, M.; Noé, F.; Kaupp, U. B.; Seifert, R. Kinetics of Ligand-Receptor Interaction Reveals an Induced-Fit Mode of Binding in a Cyclic Nucleotide-Activated Protein. *Biophys. J.* **2013**, *104* (1), 63−74.
(65) Haran, G.; Haas, E.; Szpikowska, B. K.; Mas, M. T. Domain motions in phosphoglycerate kinase: determination of interdomain distance distributions by site-specific labeling and time-resolved fluorescence energy transfer. *Proc. Natl. Acad. Sci. U. S. A.* **1992**, *89* (24), 11764−11768.
(66) Joseph, B.; Jaumann, E. A.; Sikora, A.; Barth, K.; Prisner, T. F.; Cafiso, D. S. In situ observation of conformational dynamics and protein ligand-substrate interactions in outer-membrane proteins with DEER/PELDOR spectroscopy. *Nat. Protoc.* **2019**, *14* (8), 2344−2369.
(67) Fürtig, B.; Buck, J.; Manoharan, V.; Bermel, W.; Jäschke, A.; Wenter, P.; Pitsch, S.; Schwalbe, H. Time-resolved NMR studies of RNA folding. *Biopolymers* **2007**, *86* (5−6), 360−383.

## NOTE ADDED AFTER ISSUE PUBLICATION

This article was initially published with an incorrect copyright statement and was corrected on or around May 28, 2021.


https://doi.org/10.1021/jacs.1c01081
J. Am. Chem. Soc. 2021, 143, 6981−6989